Heliyon 9 (2023) e18531

Contents lists available at ScienceDirect

Heliyon

journal homepage: www.cell.com/heliyon

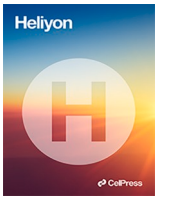

An ab-initio study of P-type ZrCoY (Y═Sb and Bi) half – Heusler semiconductors

Lynet Allan [a,*], Winfred M. Mulwa [b], Julius M. Mwabora [a], Robinson J. Musembi [a], R.E. Mapasha [c]

[a] Department of Physics, Faculty of Science and Technology, University of Nairobi, P.O.Box 30197-00100, Nairobi, Kenya
[b] Department of Physics, Faculty of Science, Egerton University, P.O Box 536-20115, Egerton, Kenya
[c] Department of Physics, University of Pretoria,Private Bag x 20, Hatfield, South Africa

ARTICLE INFO

Keywords:
First principles
Electronic
Mechanical
Optical and thermoelectric properties
Half-Heusler alloys
ZrCoY (Y = Sb and Bi)

ABSTRACT

In this study, the structural, electronic, mechanical, optical, and thermoelectric properties of the cubic half-Heusler compound ZrCoY(Y═Sb and Bi) obtained using first-principles calculations are presented. The following exchange-correlation functionals have been employed: Generalized Gradient Approximation with Perdew-Burke-Ernzerhoff (GGA-PBE), Generalized Gradient Approximation with Perdew-Burke-Enzerhoff for solids (GGA-PBESol) and Local Density Approximation (LDA). Both ZrCoSb and ZrCoBi compounds are mechanically and dynamically stable, based on the elastic and phonon properties analysis. The calculated electronic band gaps for both compounds are about 1 eV, as predicted by all the three functionals. Since it is noted that GGA-PBE functional is most favourable for predicting structural properties and the energetic stability of ZrCoSb and ZrCoBi compounds, it is further used to calculate their thermoelectric properties. Within the energy range of 0–40 eV, the refractive index, dielectric constant, and energy loss function of ZrCoSb and ZrCoBi compounds are calculated. The possibility of electronic transition from the valence band maximum (VBM) to the conduction minimum band (CBM) is confirmed by the occurrence of absorption peaks in the visible range. For the evaluation of thermoelectric properties, the p-type and n-type doping attained Seebeck coefficients of 1800 and -1800 μVK^{-1} at 300 K, respectively. The maximum peak of 17 $\times$ 10^{11} W/m s K^2 is attained in n-type doping, according to the power factor results.

1. Introduction

Heusler compounds have made substantial progress in the field of materials science [1,2]. Due to their properties, including half metallicity, superconductivity, the Hall effect, ferromagnetism, and thermoelectricity, these substances have attaracted alot of attention [1–6]. However, a Heusler alloy's stability plays a significant role in evaluating whether or not it is appropriate for a certain application. According to Born, one way to confirm a structure's overall stability is to evaluate its mechanical stability through theoretical calculations [6]. Density functional theory and the semi-classical Boltzmann approach have been used in some research on half-Heusler (HH) substances [7–9]. The remarkable thermoelectric properties of MCoSb compounds (M = Ti, Zr, and Hf) were recently found by Sekimoto and his team through experimental research. Their findings were in agreement with previously published

* Corresponding author.
E-mail address: lynetamondi3@gmail.com (L. Allan).

https://doi.org/10.1016/j.heliyon.2023.e18531
Received 1 May 2023; Received in revised form 19 July 2023; Accepted 20 July 2023
Available online 26 July 2023

experimental and computational results [10,11]. Additionally, MNiSn-based HH alloys (M = Ti, Zr, and Hf) have shown promise as thermoelectric device materials [12,13]. When compared to other alloys, Zr-based HH alloys show the highest figure of merit (ZT=0.8). However, there hasn't been a lot of investigation into the stability of MNiSn and MCoSb HH alloys using various exchange and correlation functionals. Coban et al. (2016) examined the elastic constants of HfCoSb within the context of density functional theory using a particular kind of exchange and correlation approximation [14].

We are particularly interested in ZrCoSb, one of the MCoSb HH alloys, and we further substitute Sb with Bi to see how this substituition affects its characteristics. Zirconium (Zr), cobalt (Co), and antimony (Sb) atoms make up the compound ZrCoSb. It has intriguing magnetic characteristics, especially a spin-polarized [3,15] ferromagnetic nature. The majority of its electron spins are aligned in parallel, indicating that it has spontaneous magnetization. Different characterisation methods, such as magnetization measurements, specific heat measurements, and neutron scattering investigations, provide experimental support for the spin-polarized ferromagnetic nature of ZrCoSb [10,16].

To our knowledge, no theoretical research has been done on the selection of exchange and correlation functionals for examining the physical properties of HH compounds. Additionally, these two compounds' optical properties have not yet been studied. When determining whether these compounds are suitable for solar energy harvesting, the optical properties—which include the real and imaginary dielectric constants, refractive index, reflectivity, and energy loss function—play a key role. We present a thorough analysis of the thermoelectric characteristics of ZrCoY (Y=Sb, Bi) compounds in this paper. In thermoelectric (TE) devices, the electrical conductivity (σ), thermal conductivity (K), and Seebeck coefficient (S), which are all temperature-dependent and affect the material's usefulness, all have an impact on the device's efficiency. The figure of merit (ZT), which is defined by equation (1), represents the maximum efficiency of the energy conversion process in the material at a specific temperature point.

$$ZT = \frac{S^2\sigma}{K}\mathrm{T} \tag{1}$$

K in this context refers to thermal conductivity, which often includes contributions from the electronic and lattice layers ($K_{el} + K_l$). Electrical conductivity is represented by, temperature is represented by T, and S is the Seebeck coefficient.

The cubic half-Heusler compound ZrCoY's structural, electrical, optical, and thermoelectric properties are all carefully examined in this paper. It is discovered that the compound demonstrates mechanical and dynamic stability using first principles calculations. Approximately 1 eV is found to represent the electronic band gaps, with little variance between functionals. Based on structural characteristics, the PBE functional produces the best forecast. Within the energy range of 0–40 eV, computations are made to determine the dielectric constant, refractive index, and energy loss function. The transition of electrons between the valence and conduction bands is confirmed by the visible absorption peaks. By utilizing the BoltzTrap code to explore thermoelectric characteristics, large Seebeck coefficients and a maximum power factor peak in n-type doping are discovered. Overall, this research offers insightful knowledge on the properties and possible uses of ZrCoY molecules. The paper is set up like follows: In Section 2 we provide information on the calculations performed for future reproducibility. The detailed analysis and discussions of the results are presented in Section 3. Specifically, in Section 3.1, we discuss how the three different functionals affect the structural properties of ZrCoSb and ZrCoBi. In Section 3.2, we examine the elastic constants and mechanical properties of the studied compounds using the three functionals. The projected density of states (PDOS) and electronic band structures are explored and addressed in Section 3.3. The dynamical characteristics of the compounds, including phonon dispersions, are covered in Section 3.4. We examine the optical response and electron transport behaviour of the two alloys in Sections 3.5 and 3.6, respectively.

2. Calculations

The cubic half-Heusler compounds ZrCoSb and ZrCoBi, with equal lattice parameters a = b = c and angles $\alpha = \beta = \gamma = 90^\circ$, were simulated in this study using density functional theory (DFT) [17,18]. The quantum ESPRESSO (QE) code, which is open-source and cost-free software, was used for all calculations [19]. The local density approximation (LDA), the Perdew-Burke-Erzenhoff (PBE), and the Perdew-Burke-Erzenhoff for solids (PBESol) flavors of the generalized gradient approximation (GGA) were each used separately to account for the contribution of the core electrons . The semi-relativistic technique was utilized to analyse the semi-core states, and the energy cut-off between the valence and semi-core states was set to 50.0 Ry. In the calculations, the spin-orbit coupling was not taken into account. The electron-ion interactions were described using ultrasoft pseudopotentials [19]. After adjusting the atomic positions to get the minimal energy configuration, the cut-off energy, k-points, and lattice constant were optimized. The Birch-Murnaghan equation of state was fitted to the collected data [17], as shown in Fig. 2 (a-c) and 3(a-c)for ZrCoSb and ZrCoBi, respectively. The optimal lattice constant was determined as the minimum value of the fitted curve. The optimal lattice constants are shown in Table 2, and other physical parameters were computed using these values. Six two-dimensional supercells totalling 24 atoms were used to evaluate phonon dispersion for the lattice dynamics. Three-atom unit cells were used to build the supercells, with one Zr, one Co, and one Bi/Sb atom for each of the two compounds. The Phonopy programme was used to perform finite difference phonon computations [18]. Using Quantum ESPRESSO's Thermo-PW post-processing tool, the elastic constants were calculated [16]. The Perdew-Burke-Ernzerhof Generalized Gradient Approximation (PBEGGA) was used for the thermoelectric characteristics, as indicated in Section 3.1 of this study.

3. Results and discussions

3.1. Structure of ZrCoSb and ZrCoBi

Fig. 1 illustrates the crystal structure of the half-Heusler alloy ZrCoY (Y═Sb, Bi). Zr (1/2, 1/2, 1/2), Co (1/4, 1/4, 1/4), and Y (Sb/Bi) atoms' respective Wyckoff locations are Zr (1/2, 1/2, 1/2), Co (1/4, 1/4, 1/4), and Sb/Bi (0, 0, 0). There is a gap in the fourth sub-lattice at (3/4, 3/4, 3/4) [20,21]. It consists of four intercalated face-cantered cubic (FCC) sub-lattices.

Fig. 1 shows the crystal structures of the half-Heusler alloys ZrCoY ═Table 1 contains the bond lengths that were calculated and documented. In comparison to Zr–Bi/Sb, the bond lengths between Co–Sb and Co–Sb/Bi are shorter. Overall bond lengths are short, indicating that the compounds have large bulk moduli. The computed bulk modulus values are described in Section 3.2.

In contrast to the values obtained by LDA, which are slightly underestimated, the lattice constants for ZrCoSb derived using the PBE and PBESol functionals are identical and in good agreement with the experimental values published by Sekimoto et al. at room temperature. It should also be observed that the ZrCoSb compound using all three functionals has lattice constants that are lower than those of the ZrCoBi complex, indicating a small strain on the Co/Zr atoms from the higher mass of Bi. As the electronic band structures in Figs. 4–9 suggest that the compounds are narrow-bandgap semiconductors, it will be discussed later in this study how this difference affects the local bonding between the atoms and the resulting electronic structures. The fitted curve's minimal value, as shown in Fig. 2 (a–c) and Fig. 3(a–c) for ZrCoSb and ZrCoBi, respectively, was used to determine the optimal lattice constant.

When computed using PBE and PBESol, the lattice constants for ZrCoSb are essentially identical and correspond fairly well with the experimental values of 6.0676 a.u reported by Sekimoto et al. [3] but those produced using LDA are slightly exaggerated, as seen in Table 2, at room temperature. It should also be noted that the ZrCoSb combination, which uses all three functionals, has lower lattice constants than ZrCoBi, indicating that the larger mass of Bi caused a minor strain on the Co/Zr atoms. PBE calculations, on the other hand, had the lowest ground state energy and the highest equilibrium V_0, making them the preferred functional for calculating the physical characteristics of Zr-based Half Heusler alloys.

3.2. Elastic constants and mechanical properties

Different elastic parameters of both ZrCoY compounds are calculated from the elastic constants using the Voigt Reuss, and Hill averaging [3,22,23]. The obtained elastic constants are shown in Table 3. The presented elastic constants values

of both compounds indicate that the Born-Huang stability criterion ($C_{11} > 0$, $C_{44} > 0$, $C_{11}–C_{12} > 0$, and $C_{11} + 2C_{12} > 0$) is satisfied. Therefore, it is predicted that the HH compounds ZrCoY (Y═Sb, Bi) are mechanically stable. Both ZrCoY compounds have higher C_{11} values than C_{12} and C_{44}, indicating resistance to compression along the X axis.

ZrCoSb and ZrCoBi have bulk moduli of 142.2 GPa and 142.1 GPa, respectively. These values are close to those obtained using Murnaghan's equation of state (136.6 GPa and 136.1 GPa, respectively). The ZrCoSb material's high bulk modulus exhibits both its incompressibility and great bond strength. The hardness of ZrCoSb and ZrCoBi is indicated by the estimated shear moduli, which are 79.9 GPa and 71.3 GPa, respectively. Sadly, there are no elastic constants or elastic moduli data for ZrCoBi, which makes direct comparison challenging. Given that ZrCoSb has a greater Young's modulus value of 202.6 GPa compared to ZrCoBi's 183.4 GPa, ZrCoSb is stiffer than ZrCoBi. ZrCoBi and ZrCoSb are both ductile materials, according to the Pugh ratio (B/G), which has a value of 1.77 and 1.99, respectively. For Poisson's ratio (v) to be more than 0.26, it denotes ductility; otherwise, it denotes brittleness.

Since ZrCoSb's predicted Young's, modulus is greater than the observed data, covalent bonding appears to be the most common kind of bonding. Strong covalent bonds are a sign of stiffness in a material.

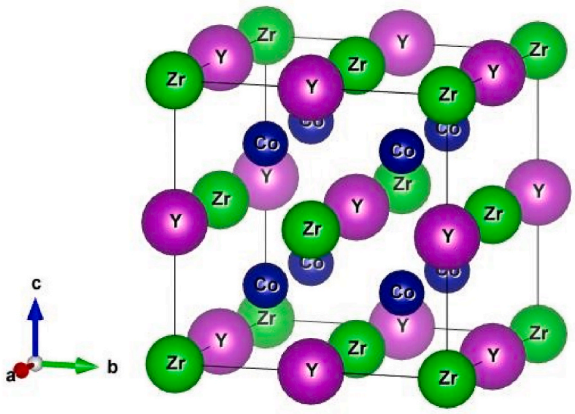

Fig. 1. The crystal structures of Half Heusler alloys ZrCoY (Y═Sb,Bi).

Table 1
Calculated bond lengths for ZrCoY (Y=Sb,Bi).

Bonds	Zr–Co	Co–Sb/Bi	Zr–Sb/Bi	XC
Bond Lengths (Å)	2.64	2.64	3.05	PBE
	2.64	2.64	3.05	PBESol
	2.97	2.97	3.43	LDA

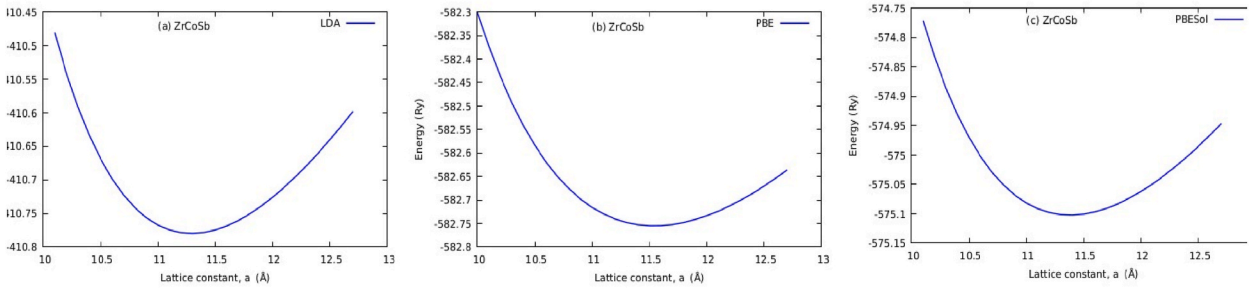

Fig. 2. Energy vs lattice constant curves for ZrCoSb using (a)LDA, (b)PBE, and (c) PBESol.

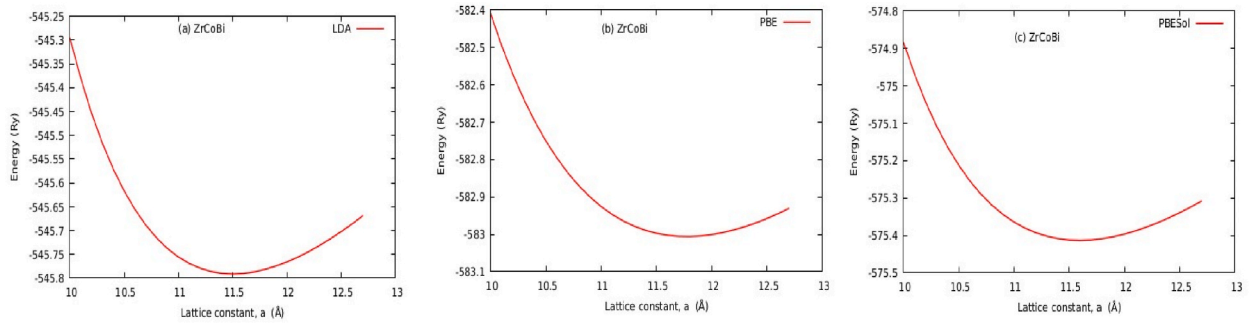

Fig. 3. Energy vs lattice constant curves for ZrCoBi using (a)LDA, (b)PBE, and (c) PBESol.

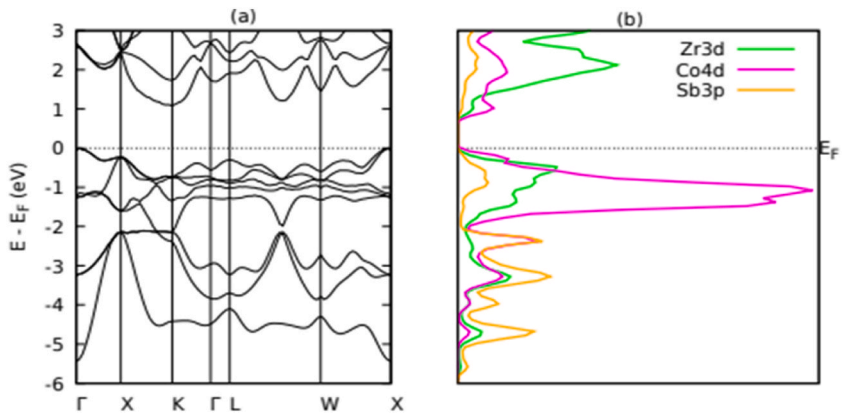

Fig. 4. (a) LDA Calculated Band structures and (b) Projected Density of States (PDOS) for ZrCoSb.

3.3. Electronic properties

The electronic band structures were calculated to examine the electronic characteristics of ZrCoBi and ZrCoSb compounds. The electronic band structures of both compounds demonstrate that they are indirect band gap semiconductors, since their VBM (CBM) appears at the K (X) high-symmetry points, as shown in Figs. 4–9. Furthermore, these calculations show that these compounds have

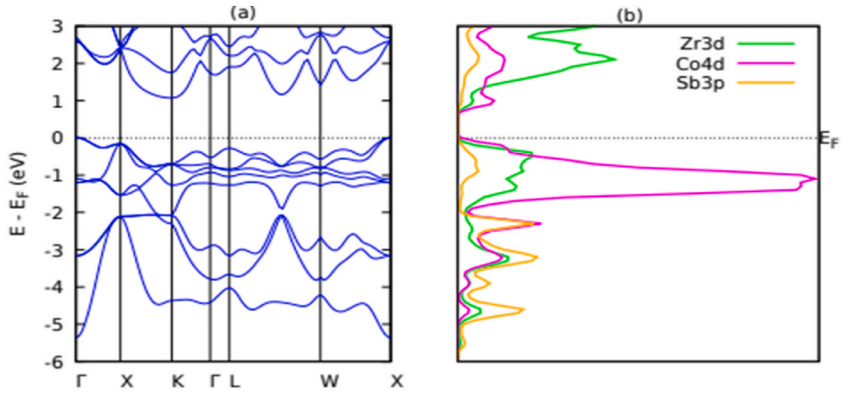

Fig. 5. (a) GGA-PBE Calculated Band structures and (b) Projected Density of States (PDOS) for ZrCoSb.

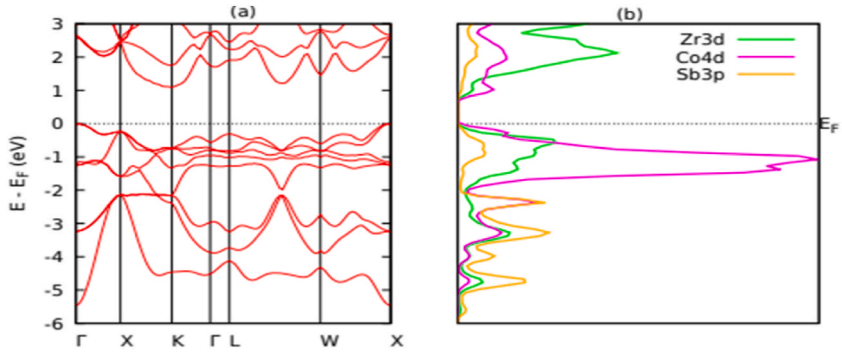

Fig. 6. (a) GGA-PBESol Calculated Band structures and (b) Projected Density of States (PDOS) for ZrCoSb.

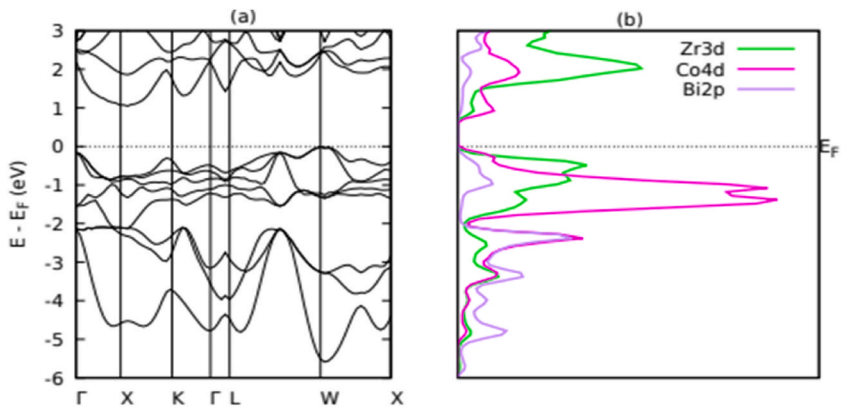

Fig. 7. (a) LDA Calculated Band structures and (b) Projected Density of States (PDOS) for ZrCoBi.

strong reflectivity in the infrared region of the photon energy spectrum. Phonon vibrations increase the conductivity of indirect bandgap semiconductors; this topic will be covered in more detail in Section 3.4, focusing on the phonon vibrational characteristics of these compounds. The band gap of the ZrCoY compounds is just above 1 eV, demonstrating their non-metallic electronic nature. Table 5 shows the magnitude of band gaps calculated from the three functionals.

Comparing the band gaps predicted by the GGA-PBESol approximation to the reported experimental values, it is clear that the latter are less accurate. However, there is a small variance between theoretically derived and experimentally measured bandgaps. There are several reasons for this. The projected bandgap can deviate because theoretical calculations frequently include approximations and assumptions that don't accurately reflect the complexity of the actual system [24]. The differences may also be a result of ignoring electrical correlations and the impact of temperature and pressure [10]. The presence of structural flaws, contaminants, and technological limitations in the experiment can potentially have an impact on the observed band structure and measured bandgap.

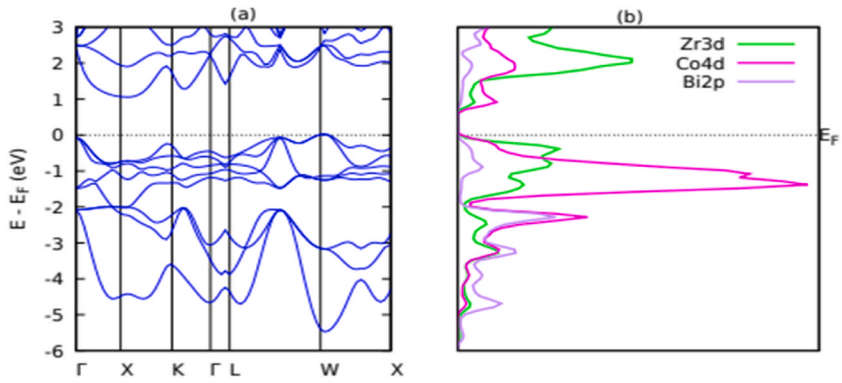

Fig. 8. (a) GGA-PBE Calculated Band structures and (b) Projected Density of States (PDOS) for ZrCoBi.

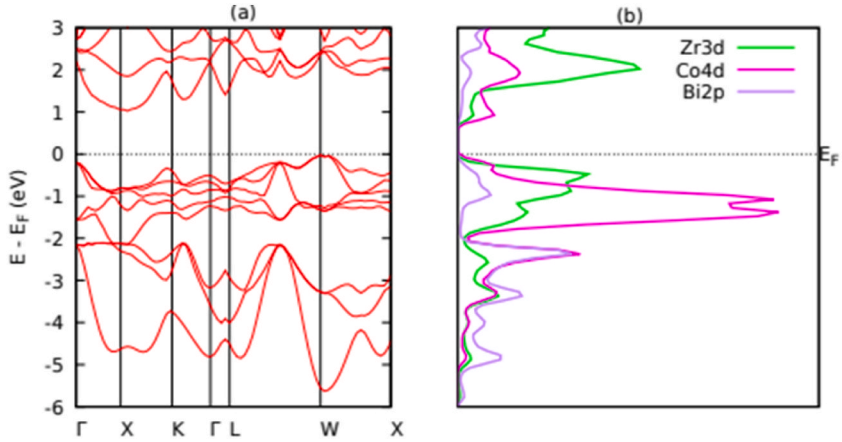

Fig. 9. (a) GGA-PBESol Calculated Band structures and (b) Projected Density of States (PDOS) for ZrCoBi.

Table 2
Calculated structural properties for ZrCoY (Y═Sb,Bi).

Structural Properties	ZrCoSb			ZrCoBi		
	LDA	PBE	PBESol	LDA	PBE	PBESol
Lattice Parameters a_0(Å)	11.293	11.546	11.367	11.490	11.775	11.596
Bulk modulus B_o(GPa)	153.8	127.6	142.6	134.4	114.8	125.4
Ground state energy E_o (Ry)	−410.77	−582.75	−575.10	−545.79	−583.00	−575.41
Equilibrium volume 358.07 V_o (a.u)^3		383.46	366.63	381.61	408.24	389.91

Table 3
The calculated Elastic Constants and Mechanical Properties of ZrCoBi and ZrCoSb compounds obtained using GGA-PBE, GGA- PBESol and LDA.

Compound	C_{11} (GPa)	C_{12}(GPa)	C_{44} (GPa)	B (GPa)	G (GPa)	B/G	E (GPa)	*n*	Θ_D	XC
>ZrCoSb		35.5	85.5	111.2	95.8	1.16	223.3	0.165	419.17	LDA
	262.3	68.1	69.7	133.3	79.9	1.66	199.8	0.250	392.12	PBE
	243.5	10.6	82.0	88.3	94.3	0.93	208.7	0.105	414.26	PBESol
ZrCoBi	198.0	56.9	75.1	69.8	82.9	0.48	178.2	0.074	340.30	LDA
	322.2	150.3	52.7	207.6	64.2	3.23	174.7	0.359	312.75	PBE
	159.6	22.8	58.3	37.9	69.8	054	129.8	0.072	308.82	PBESol

Table 4
Calculated bandgaps using LDA, PBE, and PBESol in comparison to experimental gaps.

Materials	Calculated Band gaps			
	LDA	PBE	PBESol	Expt
ZrCoSb	1.1095	1.0765	1.1123	1.45
ZrCoBi	1.0738	1.0416	1.0751	–

Table 5
Calculated static dielectric constant, optical band gap, static refractive index n (0), static reflectivity R (0), and static loss function L (0) for ZrCoSb and ZrCoBi, using LDA, PBE, and PBESol XC functionals.

Compound	XC	$\varepsilon_1(0)$	ΔE_{OG}	n (0)	R (0)	L (0)
ZrCoSb	LDA	19.3	1.26	4.391	0.395	0.000335
	PBE	19.7	1.36	4.435	0.399	0.000347
	PBESol	19.2	1.23	4.376	0.394	0.000332
ZrCoBi	LDA	20.8	1.44	4.557	0.409	0.000331
	PBE	21.1	1.55	4.593	0.413	0.000344
	PBESol	20.6	1.41	4.536	0.408	0.000330

Advanced theoretical techniques are needed to improve the agreement between theoretical and experimental bandgaps [21], which are computationally expensive.

Fig. 4b through Fig. 9(b) 's projected densities of states show that Zr predominates in the alloys' valence and conduction bands. But in ZrCoBi, Bi dominates in the valence band at energies between −6 and −2 eV. In addition, ZrCoBi exhibits a dramatic rise in state density close to the valence band maximum, which denotes a high thermal power. Table 4 provides a comparison between experimental bandgaps and bandgaps derived from the three functionals, namely LDA, PBE, and PBESol.

3.4. Lattice dynamics

The thermodynamic stability, phase transitions, and potential effects on a material's physical properties can all be considered when interpreting the phonon curve [23,24]. Here, the behaviour and features of the material's internal lattice vibrations are taken into account [34]. Quantized lattice vibrations called phonons are essential in determining the thermal and mechanical behaviour of solids,

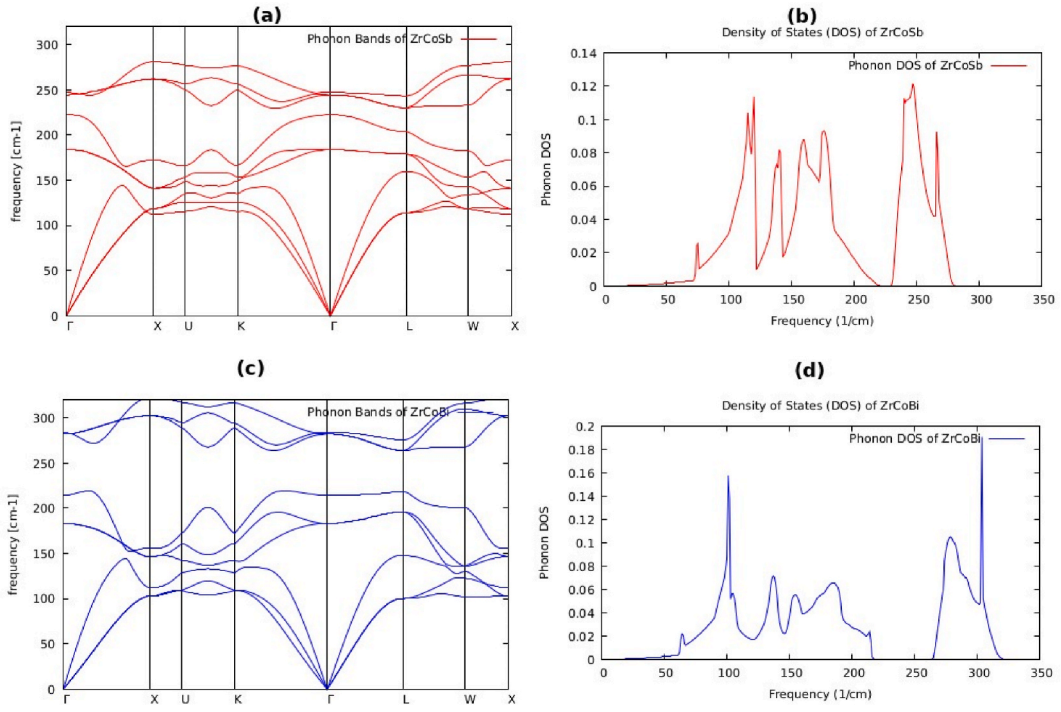

Fig. 10. The computed phonon dispersion curves and densities of states for ZrCoSb and ZrCoBi.

among other features. The phonon curve for thermodynamic stability sheds light on a material's stability by analysing the frequencies and intensities of its vibrational modes [24].

A stable substance often displays a clear, continuous phonon spectrum free of phantom frequencies. The lack of fictitious frequencies proves that the lattice vibrations are genuine and do not cause instability or decay.

Phonons significantly affect a material's physical characteristics. The phonon spectrum, for instance, has a significant impact on the thermal conductivity and thermal expansion coefficients due to modifications to the lattice structure or phase transitions that change the phonon curve [25]. In addition, excitation interactions between electrons and phonons can change material's band structure leading to alteration in electronic characteristics. Resulting in phenomena like electron-phonon coupling and the formation of superconductivity or other electronic phase transitions.

Understanding a material's thermodynamic stability, phase transitions, and potential effects on its physical properties can be done by interpreting a phonon curve. Based on phonon spectrum, researchers can better understand a material's stability, phase transitions, mechanical, and electrical properties by examining the frequencies, intensities, and behaviour of lattice vibrations. In this study, the phonon dispersions were established, and the dynamical stability was examined. These calculations were carried out using Phonopy and the Quantum ESPRESSO package. Fig. 10s findings show that neither compound's cubic phonon spectrum has any imaginary frequencies, supporting the compounds' dynamical stability. Lattice vibration research sheds light on how solids absorb energy. The estimated phonon dispersion curves and state densities for ZrCoSb and ZrCoBi are shown in Fig. 10(a)–(d).

A general method can be used to choose the optical and acoustic modes from a phonon dispersion curve. We start by locating the low-frequency portion of the curve for acoustic modes. Then, branches near high-symmetry sites, like the -point, that show a linear or quadratic dispersion should be taken into account. Compared to optical modes, acoustic modes often propagate at lower frequencies and wavevectors. Therefore, the longitudinal (LA) and two transverse (TA) modes, which are the lowest-frequency and low-wave vector acoustic modes, can be represented by three branches [18]. On the other hand, one should concentrate on branches showing a nonlinear dispersion curve for optical modes. When compared to acoustic modes, optical modes typically propagate at higher wave-vectors and frequencies. So, it makes sense that branches that differ from the linear or quadratic behaviour seen in acoustic modes are of interest. Our studied longitudinal optical (LO) and two transverse optical (TO) modes is represented by choosing the six branches corresponding to the highest-frequency and high-wavevector optical modes. These recommendations make it easier to recognize and categorize acoustic and optical modes from the phonon dispersion curve [23].

When compared to acoustic modes, optical modes typically propagate at higher wave-vectors and frequencies. So, it makes sense that branches that differ from the linear or quadratic behaviour seen in acoustic modes are of interest. The LO and two TO modes can be represented by choosing the six branches corresponding to the highest-frequency and high-wavevector optical modes. These recommendations make it easier to recognize and categorize acoustic and optical modes from the phonon dispersion curve.

3.5. Optical properties

Solids' optical characteristics can be used to illustrate how they interact with light. The parametrized dielectric function $\varepsilon(\omega)$ reflects how physically material's electrons react to electromagnetic radiation. Equation (2) separates $\varepsilon(\omega)$ in terms of real portion $\varepsilon 1$ (ω) and imaginary potion $\varepsilon 2(\omega)$.

$$\varepsilon(\omega) = \varepsilon_1(\omega) + i\varepsilon_2(\omega) \tag{2}$$

Other optical quantities such as absorption ($\alpha(\omega)$) using equation (3) and refractivity ($n(\omega)$) using equation (4) mainly come from $\varepsilon_1(\omega)$ and $\varepsilon_2(\omega)$. Equation (5) is used for derivation of extinction coefficient ($K(\omega)$), (6) is used for the loss function ($L(\omega)$ and (7) derive the reflectivity ($R(\omega)$).

$$\alpha(\omega) = \left(\sqrt{\varepsilon_1^2(\omega) + \varepsilon_2^2(\omega)} - \varepsilon_1(\omega)\right)^{1/2} \tag{3}$$

$$n(\omega) = \sqrt{2\omega}\left(\frac{\sqrt{\varepsilon_1^2(\omega) + \varepsilon_2^2(\omega)} - \varepsilon_1(\omega)}{2}\right)^{1/2} \tag{4}$$

$$\mathrm{k}(\omega) = \sqrt{2\omega}\left(\frac{\sqrt{\varepsilon_1^2(\omega) + \varepsilon_2^2(\omega)} - \varepsilon_1(\omega)}{2}\right)^{1/2} \tag{5}$$

$$\mathrm{L}(\omega) = \frac{\varepsilon_2(\omega)}{\varepsilon_1^2(\omega) + \varepsilon_2^2(\omega)} \tag{6}$$

$$\mathrm{R}(\omega) = \frac{(n-1)^2 + K^2}{(n+1)^2 + K^2} \tag{7}$$

From the above equations, the following relations were obtained.

The $\varepsilon_2(\omega)$ describes absorption of a photon in our ZrCoSb and ZrCoBi compounds materials. The noted sharp peaks in the $\varepsilon_2(\omega)$ curves are used to indicate the electronic transitions from the VBM to CBM of ZrCoSb and ZrCoBi. The band gaps of the ZrCoSb and

ZrCoBi materials that fall within the visible region (<3.1 eV) are indicated by the commencement of the absorption in the α(ω) curves shown in Fig. 11(c) and Fig. 12(c).

Strong inter-band transitions are indicated by the band gaps for ZrCoSb and ZrCoBi employing the three functionals, which range from 1.23 eV to 1.55 eV in Table 5 (see Fig. 13). ZrCoSb and ZrCoBi are appealing alternatives for solar applications because of these band gaps. Additionally, compared to wider band gaps, narrower band gaps enable faster electron transitions [26]. The gaps in the bands line up with the spaces in the band structures.

The static value $\varepsilon_1(\omega)$ (at energy = 0 is a crucial aspect of the $\varepsilon_1(\omega)$ curve. There is a relationship between this static value and n(ω) of the substance. Figs. 11(a) and Figure 12(a) show the primary peaks of the $\varepsilon_1(\omega)$ plot for ZrCoSb and ZrCoBi, respectively, in energy regions greater than 1.5 eV and 2.7 eV, starting at energy (0). Photon transmission continues in the 8–12 eV energy range until the $\varepsilon_1(\omega)$ values go negative. In this energy area, we notice the full attenuation of the incident photon radiations, and the ZrCoSb and ZrCoBi compounds behave semi-metallically, according to Murtaza (2011) [27].

Table 5 lists the calculated various refractive indices that are obtained at zero energy level from the n(ω) curves in Figs. 11(c) and Figure 12(c). In the visible zone, the primary refractive index peaks are observed. Strong optical absorption is seen in the low energy range of 3.0 eV–3.2 eV for ZrCoSb and ZrCoBi. These compounds' optical absorption coefficients span the UV–Vis regions, indicating that they are appropriate for photovoltaic applications.

These compounds are well suited for solar applications since the calculated absorption coefficients in the energy range of 2.0 eV–13.6 eV cover a sizable section of the electromagnetic spectrum. The surface behaviour of the materials and the energy loss caused by quickly entering electrons are determined by the reflectivity curves shown in Figs. 11(d) and Figure 12(d), as well as the *L* curves shown in Fig. 12(b) and (b). The principal reflectivity peaks for ZrCoSb and ZrCoBi are located in the energy ranges of 6 eV–11 eV and 2 eV–6 eV, respectively, according to each of the three functionals. Reflectance decreases beyond these boundaries.

Both compounds' loss spectra in Fig. 12(b) and (b) don't exhibit any appreciable visual absorption. ZrCoSb and ZrCoBi have principal absorption peaks that are located at higher energies (respectively, >12 eV and >10 eV). Unfortunately, a direct comparison of the optical results cannot be made since ZrCoBi lacks experimental and theoretical data. However, the optical results obtained for ZrCoSb are consistent with those published by Chauhan et al. [10]. Fig. 11(e) and (e) show the refractivity n (0), while Fig. 11(f) and (f) show the extinction coefficient K (.), for ZrCoSb and ZrCoBi, respectively. Table 5 lists the computed static refractive indices n (0), optical band gaps ΔE_{OG}, and static dielectric constants ε_1 (0).

3.6. Thermoelectric properties

The thermoelectric properties of ZrCoSb and ZrCoBi have been computed using the Boltzmann transport model, which is implemented in the BoltzTrap code, throughout the temperature range of 300–800 K. The Seebeck coefficient (S), electrical conductivity (K_e), power factor (PF), and dimensionless Figure of Merit (ZT) are some of the thermoelectric parameters that are covered in this study.

Fig. 14 demonstrates how changes in temperature and energy affect the electrical conductivity and electronic conductivity over time. With a gradient that is steeper for positively increasing energies than for more decreasing energies, both compounds exhibit the same pattern. This demonstrates that although n-type compounds carry electricity, they have poorer electronic conductivity than p-type ones.

The electronic and electrical conductivity per relaxation time is zero in the energy range between −0.5 and + 0.5; above this range, it increases in both cases.

The Seebeck coefficient, a measure of thermoelectric efficiency, increases initially with increasing energy, reaches a maximum value, and then decreases drastically. The Seebeck coefficient peaks are in the energy ranges of −0.5 to +0.5, as shown by Fig. 15(a and b). The curves often reach zero beyond this area. Both n-type and p-type ZrCoSb alloys have their highest peak doping at 1500 $V\mu K^{-1}$. The ZrCoY alloy has good thermoelectric characteristics since the peaks are still discernible at 800 K. . The heights of the peaks often decrease as the temperature rises. These alloys have the potential to be used in thermoelectric applications because their computed Seebeck coefficient values are equivalent to those of other half-Heusler alloys like MCoSb (M = Ti, Zr, and Hf) and MNiSn (M = Ti, Zr, Hf).

The power factor, which affects the overall performance of thermoelectric materials, is demonstrated by the change in power factor with energy at different temperatures in Fig. 15(c and d). ZrCoSb and ZrCoBi both perform well as thermoelectric materials based on their power factors. The maximum power factor is reached for n-type doping at 800 K at 17×10^{11} W/m s K^2, whereas for p-type doping at 800 K it is at 9×10^{11} W/m s K^2.

Maximum power factors of 1.8×10^{11} W/m s K^2 and 2×10^{11} W/m s K^2 for n-type and p-type ZrCoSb at 300 K are reported, respectively. When n-type doping is used at 800 K, the greatest power factor for ZrCoBi is seen to be 19×10^{11} W/m/sK^2 and 7×10^{11} W/m/sK^2, respectively. The maximal power factors for n-type and p-type ZrCoBi at 300 K are 1.5×10^{11} W/m/sK^2 and 1.3×10^{11} W/m/sK^2, respectively. ZrCoBi has a larger power factor at 800 K than ZrCoSb, indicating that its electrons are more thermally stimulated to the conduction bands.

Therefore, ZrCoBi is a preferable option for thermoelectric (TE) applications if the power factor (PF) is thought to be a good way for reaching high efficiency (ZT) in thermoelectric materials.

Fig. 15(e and f) plots the dimensionless figure of Merit (ZT) against the chemical potential at each temperature. It is remarkable that even at room temperature, ZrCoY has a high Figure of Merit (ZT ~ 0.5). ZT has a decreasing value as temperature rises, which is explained by the large impact of phonon contribution on thermal conductivity (k). At 800 K, both compounds achieve their highest ZT, with ZT ≈ 0.85.

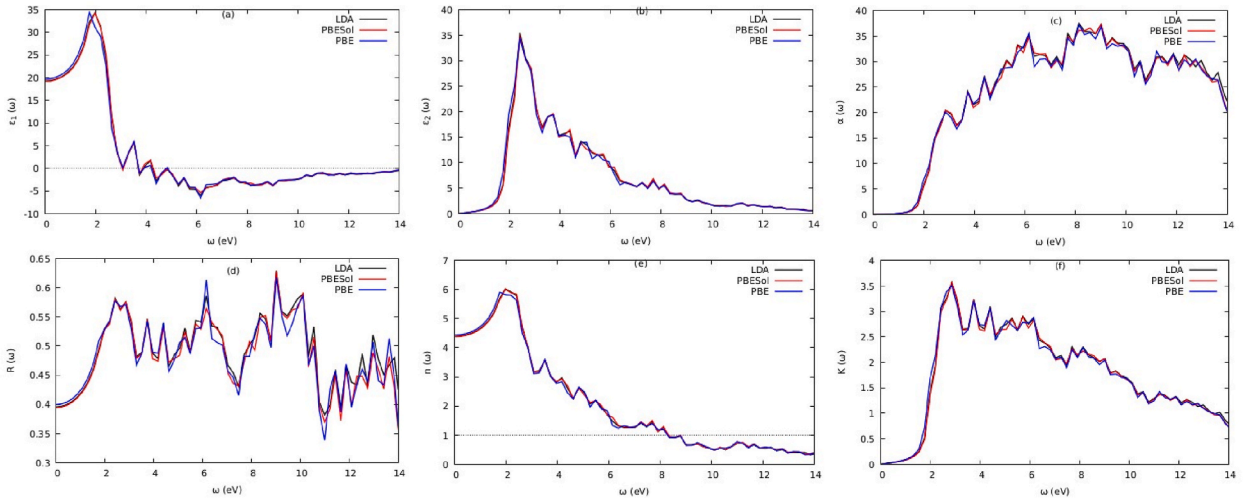

Fig. 11. Plots of separated dielectric functions; (a) (ε_1) part and (b) (ε_2) part with respect to Photon energy for ZrCoSb. The plots (c) α(ω), (d) R(ω), (e) n(ω), and (f) K(ω) vs Photon energy for ZrCoSb.

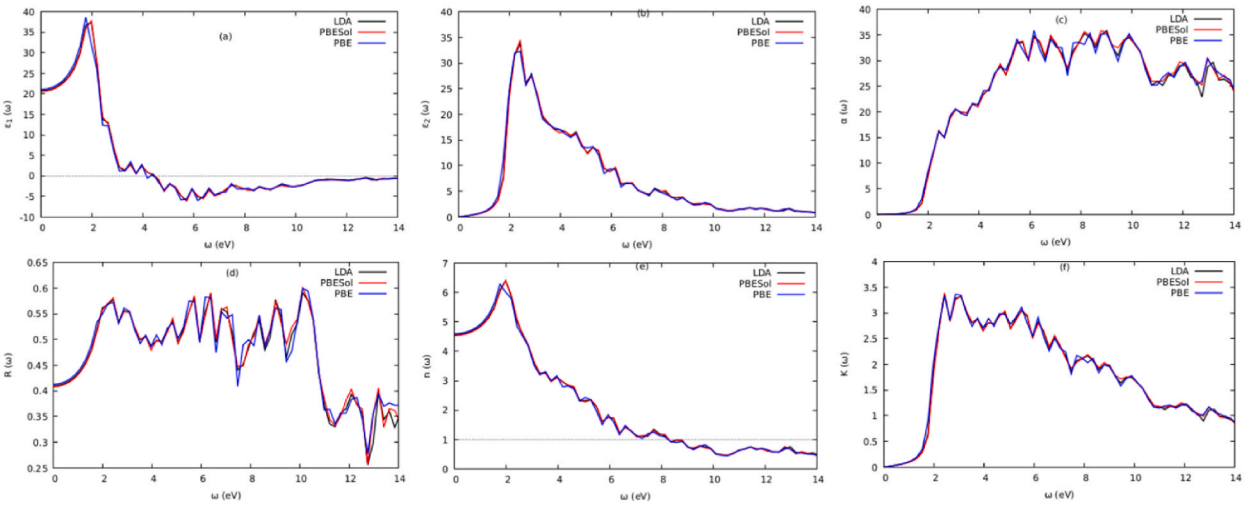

Fig. 12. Plots of separated dielectric functions; (a) (ε_1) part and (b) (ε_2) part with respect to Photon energy for ZrCoSb. The plots (c) α(ω), (d) R(ω), (e) n(ω), and (f) K(ω) vs Photon energy for ZrCoBi.

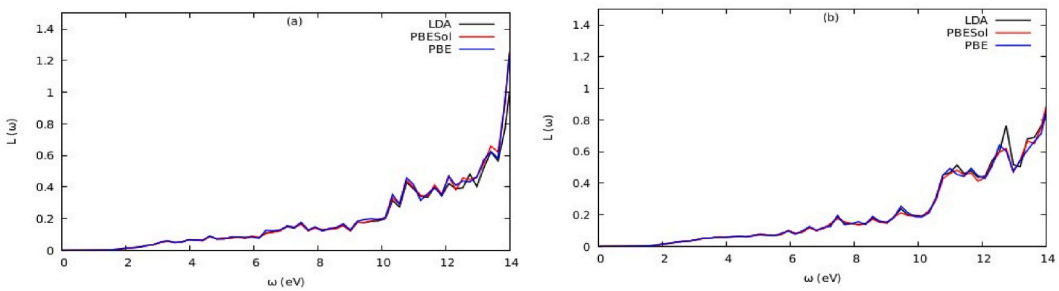

Fig. 13. Electron energy loss L for (a) ZrCoSb, and (b)ZrCoBi with respect to Photon energy.

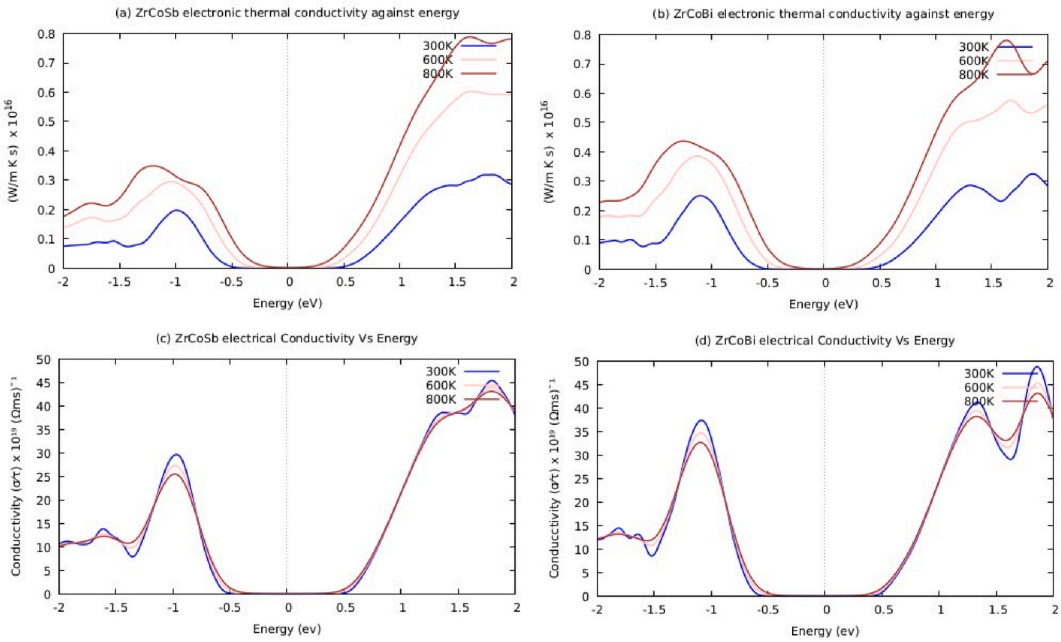

Fig. 14. (a–b) K_e and (c–d) α/τ of the ZrCoY TE materials as a function of temperature.

4. Conclusion

The half-Heusler alloys ZrCoSb and ZrCoBi have been thoroughly examined in this study in terms of their structural, electrical, mechanical, dynamical, optical, and thermoelectric properties. Density functional theory (DFT) computations were carried out utilizing the GGA-PBE, PBESol, and LDA approximations.

For elastic constants, mechanical properties, electronic band gaps, and optical properties, the results from the three approaches were in fair agreement with one another and with the experimental data that was at hand. The GGA-PBE approximation, however, produced the lowest ground state energies for both ZrCoY compounds, demonstrating its applicability for computing the half-Heusler family's physical properties.

The material's mechanical properties were confirmed by the computed values for bond strength, hardness, and stiffness as well as by the bulk modulus, shear modulus, and Young's modulus. The compounds behave as semiconductors for both electrical and optical conduction because the optical band gaps, which were calculated using the imaginary component of the dielectric function, were discovered to be near to the energy band gaps. The optical characteristics changed with photon energy, pointing to possible optoelectronic and thin film growth applications.

By calculating the Seebeck coefficient, electrical conductivity, power factor, and dimensionless Figure of Merit (ZT), ZrCoSb/Bi alloys' thermoelectric performance was studied . At 300 K, the Seebeck coefficients for the n-type and p-type doping were 1800 and -1800 μVK^{-1}, respectively. In n-type doping, the greatest power factor peak of 17×10^{11} W/msK^2 was obtained . At 800 K, the ZT value for the ZrCoY alloy was found to be high (0.85). Because of these compounds' advantageous optical and thermal responses, it is possible that they could be used in optoelectronic and thermodynamic devices.

Author contribution statement

Lynet Allan, Winfred M. Mulwa, Julius M. Mwabora, Robinson J. Musembi and R.E Mapasha: Conceived and designed the analysis, analyzed and interpreted the data, contributed analysis tools, and wrote the paper.

Data availability statement

Data will be made available on request.

Additional information

No additional information is available for this paper.

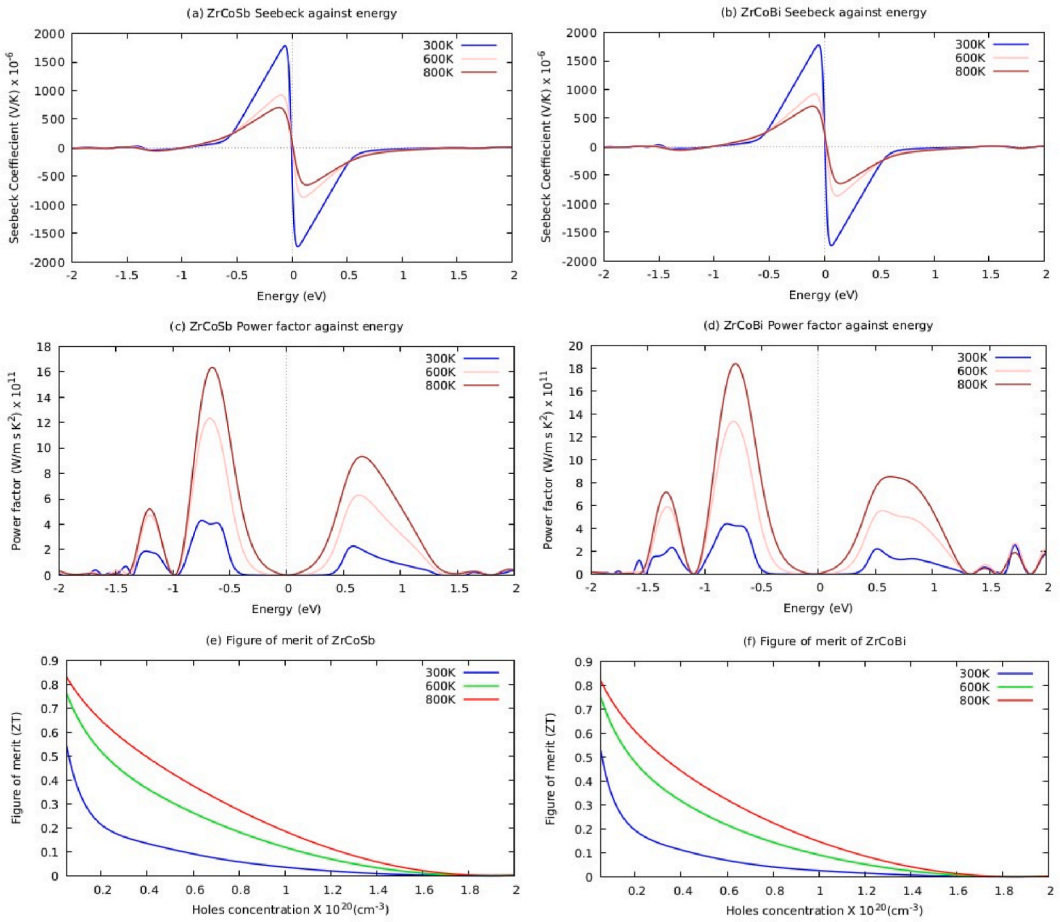

Fig. 15. (a–b) Seebeck coefficient, (c–d)} PF, and (e–f) ZT as a function of temperature using GGA for the ZrCoY, TE materials as a function of temperature.

Funding statement

The Partnership for Skills in Applied Sciences, Engineering, and Technology (PASET), through its Regional Scholarship and Innovation Fund(RSIF), provided financial support to the authors. The Centre for High Performance Computing (CHPC), located in Cape Town, South Africa, is also appreciated by the authors for providing the HPC cluster facility used in this study. The support from the University of Pretoria is also acknowledged.

Declaration of competing interest

The authors declare that they have no known competing financial interests or personal relationships that could have appeared to influence the work reported in this paper.

References

[1] A. Adewale, C. Abdullah, First principles enhanced electronic band structure of SrTiO3 using DFT+U method, International Journal of Nanoelectronics and Materials 12 (Jan. 2019) 11–18.

[2] T. Graf, C. Felser, S.S. Parkin, Simple rules for the understanding of Heusler compounds, Prog. Solid State Chem. 39 (1) (2011) 1–50 [Online]. Available: https://www.sciencedirect.com/science/article/pii/S0079678611000021.

[3] T. Sekimoto, K. Kurosaki, H. Muta, S. Yamanaka, Thermoelectric and thermophysical properties of Ticos-ZrCoSb-HfCoSb pseudo ternary system prepared by spark plasma sintering, Mater. Trans. 47 (6) (2006) 1445–1448 [Online]. Available: https://www.jstage.jst.go.jp/article/matertrans/47/6/47_6_1445/_article/-char/ja/.

[4] J. Wei, G. Wang, Thermoelectric and optical properties of half-Heusler compound TaCoSn: a first-principle study, J. Alloys Compd. 757 (2018) 118–123 [Online]. Available: https://www.sciencedirect.com/science/article/pii/S0925838818317158.

[5] D. Young, P. Khalifah, R.J. Cava, A. Ramirez, Thermoelectric properties of pure and doped FeMSb (M= V, Nb), J. Appl. Phys. 87 (1) (2000) 317–321 [Online]. Available: https://aip.scitation.org/doi/abs/10.1063/1.371863.

[6] D. Rai, A. Shankar, M. Sandeep, Ghimire, R. Thapa, Electronic structure and magnetic properties of Co 2 YZ (Y= Cr, Z= Al, Ga) type Heusler compounds: a first principle study, Int. J. Mod. Phys. B 26 (8) (2012), 1250071 [Online]. Available, https://www.worldscientific.com/doi/abs/10.1142/S0217979212500713.
[7] W. Jeitschko, Transition metal stannides with MgAgAs and MnCu2Al type structure, Metall. Trans. A 1 (11) (1970) 3159–3162.
[8] W.-S. Liu, et al., Thermoelectric property studies on Cu-doped n-type CuxBi2Te2. 7Se0. 3 nanocomposites, Adv. Energy Mater. 1 (4) (2011) 577–587 [Online]. Available: https://onlinelibrary.wiley.com/doi/abs/10.1002/aenm.201100149.
[9] T.M. Tritt, Thermal Conductivity: Theory, Properties, and Applications, Springer Science & Business Media, 2005 [Online]. Available: https://books.google.com/books?hl=en&lr=&id=whJNfKmziiIC&oi=fnd&pg=PA1&dq=gang,+2005+thermal+conductivity&ots=rzKzZDFoZV&sig=wF43jNNUWKx4PAW_u-2xqXvjh8w.
[10] N.S. Chauhan, et al., Enhanced thermoelectric performance in p-type ZrCoSb based half-Heusler alloys employing nanostructuring and compositional modulation, Journal of Materiomics 5 (1) (2019) 94–102 [Online]. Available: https://www.sciencedirect.com/science/article/pii/S2352847818300972.
[11] C. Uher, J. Yang, S. Hu, D.T. Morelli, G.P. Meisner, Transport properties of pure and doped MNiSn (M=Zr, Hf), Phys. Rev. B 59 (13) (Apr. 1999) 8615–8621, https://doi.org/10.1103/PhysRevB.59.8615.
[12] F. Aliev, Gap at Fermi level in some new d-and f-electron intermetallic compounds, Phys. B Condens. Matter 171 (1–4) (1991) 199–205 [Online]. Available: https://www.sciencedirect.com/science/article/pii/092145269190516H.
[13] S. Sakurada, N. Shutoh, Effect of Ti substitution on the thermoelectric properties of (Zr, Hf) NiSn half-Heusler compounds, Appl. Phys. Lett. 86 (8) (2005), 082105 [Online]. Available: https://aip.scitation.org/doi/abs/10.1063/1.1868063.
[14] W. Kohn, L.J. Sham, Self-consistent equations including exchange and correlation effects, Phys. Rev. 140 (4A) (1965), https://doi.org/10.1103/PhysRev.140.A1133. A1133–A1138, Nov.
[15] T. Graf, S.S. Parkin, C. Felser, Heusler compounds—a material class with exceptional properties, IEEE Trans. Magn. 47 (2) (2010) 367–373 [Online]. Available: https://ieeexplore.ieee.org/abstract/document/5654590/.
[16] D. Zhao, L. Wang, L. Bo, D. Wu, Synthesis and thermoelectric properties of Ni-doped ZrCoSb half-Heusler compounds, Metals 8 (1) (2018) 61 [Online]. Available: https://www.mdpi.com/254598.
[17] F. Murnaghan, The compressibility of media under extreme pressures, Proceedings of the national academy of sciences of the United States of America 30 (9) (1944) 244.
[18] A. Togo, I. Tanaka, First principles phonon calculations in materials science, Scripta Mater. 108 (2015) 1–5 [Online]. Available: https://www.sciencedirect.com/science/article/pii/S1359646215003127.
[19] P. Giannozzi, et al., Quantum ESPRESSO: a modular and open-source software project for quantum simulations of materials, J. Phys. Condens. Matter 21 (39) (Sep. 2009), 395502, https://doi.org/10.1088/0953-8984/21/39/395502.
[20] A.A. Adewale, A. Chik, First principles enhanced electronic band structure of SrTiO3 using DFT+ U method, INTERNATIONAL JOURNAL 12 (1) (2019) 11–18 [Online]. Available: https://ijneam.unimap.edu.my/images/PDF/Jan.
[21] A. Marzouk, M.E. Alikhani, B. Madebène, B. Tremblay, J.-P. Perchard, Vibrational spectra and structures of Ti–N2O and OTi–N2: a combined IR matrix isolation and theoretical study, J. Phys. Chem. 117 (8) (2013) 1697–1705.
[22] R. Hill, The elastic behaviour of a crystalline aggregate, Proc. Phys. Soc. 65 (5) (1952) 349 [Online]. Available: https://iopscience.iop.org/article/10.1088/0370-1298/65/5/307/meta.
[23] D. Chung, W. Buessem, The voigt-reuss-hill approximation and elastic moduli of polycrystalline MgO, CaF2, β-ZnS, ZnSe, and CdTe, J. Appl. Phys. 38 (6) (1967) 2535–2540 [Online]. Available: https://scholar.googleusercontent.com/scholar.bib?q=info:Ikib57eGNhcJ:scholar.google.com/&output=citation&scisdr=CgVAeMUUEODwnOY-a-o:AAGBfm0AAAAAY344c-omWKseUkrWqzWyRBnCsqglLmyo&scisig=AAGBfm0AAAAAY344c_GRtMVlwTvbhIvw8ZcN61wj3Z2P&scisf=4&ct=citation&cd=-1&hl=en.
[24] K. Burke, "The abc of dft," Department of Chemistry, University of California 40 (2007).
[25] Y. Wu, P. Lazic, G. Hautier, K. Persson, G. Ceder, First principles high throughput screening of oxynitrides for water-splitting photocatalysts, Energy Environ. Sci. 6 (1) (2013) 157–168 [Online]. Available: https://pubs.rsc.org/en/content/articlehtml/2013/ee/c2ee23482c.
[26] M. Samat, A. Ali, M. Taib, O. Hassan, M. Yahya, Hubbard U calculations on optical properties of 3d transition metal oxide TiO2, Results Phys. 6 (2016) 891–896 [Online]. Available: https://scholar.google.com/scholar?hl=en&as_sdt=0.
[27] G. Murtaza, I. Ahmad, First principle study of the structural and optoelectronic properties of cubic perovskites CsPbM3 (M= Cl, Br, I), Phys. B Condens. Matter 406 (17) (2011) 3222–3229 [Online]. Available: https://www.sciencedirect.com/science/article/pii/S0921452611005023.